INTERNATIONAL JOURNAL FOR NUMERICAL AND ANALYTICAL METHODS IN GEOMECHANICS
Int. J. Numer. Anal. Meth. Geomech. 2009; **33**:215–243
Published online 12 May 2008 in Wiley InterScience (www.interscience.wiley.com). DOI: 10.1002/nag.710

On a multilaminate model for soil incorporating small strain stiffness

Florian Scharinger[1,2], Helmut F. Schweiger[2,*,†] and Gyan N. Pande[3]

[1]*Garber, Dalmatiner & Partner ZT-OG, Graz, Austria*
[2]*Computational Geotechnics Group, Institute for Soil Mechanics and Foundation Engineering, Graz University of Technology, Graz, Austria*
[3]*University of Wales Swansea, Swansea, U.K.*

SUMMARY

In this paper a constitutive model for soils incorporating small strain stiffness formulated in the multilaminate framework is presented. In the multilaminate framework, the stress–strain behaviour of a material is obtained by integrating the mechanical response of an infinite number of randomly oriented planes passing through a material point. Such a procedure leads to a number of advantages in describing soil behaviour, the most significant being capture of initial and induced anisotropy due to plastic flow in a physically meaningful manner. In the past, many soil models of varying degree of refinement in the multilaminate framework have been presented by various authors. However, the issue of high initial soil stiffness in the range of very small strains and its degradation with straining, commonly referred to as 'small strain stiffness', has not been addressed within the multilaminate framework. In this paper, we adopt a micromechanics-based approach to derive small strain elastic stiffness of the soil mass. Comparison of laboratory test data with results obtained from numerical simulations based on the proposed constitutive model incorporating small strain stiffness is performed to demonstrate its predictive capabilities. The model is implemented in a finite element code and numerical simulations of a deep excavation are presented with and without incorporation of small strain stiffness to demonstrate its importance in predicting profiles of deformation. Copyright © 2008 John Wiley & Sons, Ltd.

Received 26 June 2007; Revised 21 December 2007; Accepted 28 February 2008

KEY WORDS: multilaminate model; small strain stiffness; finite element method

1. INTRODUCTION

As reliable information on the expected deformation behaviour of the subsoil is of paramount importance during design and realization of geotechnical projects, various numerical methods

*Correspondence to: Helmut F. Schweiger, Computational Geotechnics Group, Institute for Soil Mechanics and Foundation Engineering, Graz University of Technology, Graz, Austria.
†E-mail: helmut.schweiger@tugraz.at

are employed in engineering practice. The construction of shallow tunnels in urban area, deep excavations for building complex underground structures or foundations carrying loads of high-rise buildings are just some of the examples where a numerical method such as the finite element method is used for analysis. Besides many other issues, the constitutive model adopted for numerical simulation plays a key role in obtaining accurate and reliable settlement profiles. Till now, there is no universal model available which describes all aspects of soil behaviour accurately, but simple linear elastic–perfectly plastic models such as the Mohr–Coulomb model are increasingly being replaced by advanced non-linear elastic–plastic constitutive models.

One class of these higher-order models is based on the multilaminate framework, where the deformation behaviour of the soil is obtained by integrating the response of an infinite number of randomly oriented 'slip planes'. Following the work of Pande and Sharma [1], a number of models for soils in multilaminate framework have been reported, e.g. [2–4].

A comprehensive model for soils was presented by Wiltafsky [5]. However, this model did not consider high initial soil stiffness in the range of very small strains and degradation of this stiffness with straining, commonly referred to as 'small strain stiffness'. It has been shown that this aspect is important in predicting deformation profiles of geotechnical structures. In this paper, a micromechanics-based approach has been used for obtaining the small strain stiffness incorporating it in Wiltafsky's model.

Section 2 gives a brief description of the multilaminate framework and the proposed multilaminate model for soil (MMS). Here, the yield and failure criteria as well as dilatancy and hardening rules are formulated on a randomly oriented plane. The derivation of the constitutive matrix is given. In Section 3, attention is focussed on the derivation of elastic parameters of the soil mass employing various theoretical contact models, based on different assumptions. Section 4 deals with the estimates of elastic parameters at small strain and their degradation (reduction) as the strain level increases. A number of physical hypotheses are considered and comparisons are made with other theoretical models as well as experimental data available in the literature. Drained triaxial tests are simulated in Section 5 and compared with the experimental results. Results of numerical simulation of a deep excavation supported by a diaphragm wall are given in Section 6. Conclusions given in Section 7 highlight the importance of considering small strain stiffness in problems where deformations or settlements are crucial.

2. MULTILAMINATE MODEL FOR SOIL

2.1. Background

The basic concept that a number of slip planes contribute to plastic flow was first proposed by Batdorf and Budiansky [6] in the context of polycrystalline materials and was extended to clays by Calladine [7]. Conceptually, the idea was already discussed by Taylor [8]. A constitutive model for jointed rock masses having a finite set of parallel planes of weakness was first proposed by Zienkiewicz and Pande [9]. Assuming that soils have an infinite number of randomly oriented sets of planes, the rock model was extended by Pande and Sharma [1] for clays and by Sadrnejad and Pande [10] for sands. MMS was developed and implemented in the commercially available finite element code Plaxis [11] by Wiltafsky [5] as a user-defined soil model. It was extended by Scharinger and Schweiger [12] and Scharinger [13] to include small strain stiffness effects. An important feature of constitutive models in the multilaminate framework is that the evolution

DOI: 10.1002/nag

of the yield surface on each sampling plane is based on the evolution of plastic strains on the corresponding planes. Thus, any deviatoric stress path induces anisotropy while it is only under hydrostatic loading that the same pre-consolidation pressure is obtained on each plane. When any deviatoric stress is applied, the state variables related to the state of the yield surface vary over the planes. An initially isotropic soil becomes anisotropic after loading when analysed within the multilaminate framework, thus it captures plastic-flow-induced anisotropy intrinsically.

2.2. Multilaminate framework

When using a constitutive model based on the multilaminate framework for numerical analyses, the overall deformation behaviour of the soil mass is obtained by the integration of the contribution of various yielding (slipping) planes. Hence, constitutive relations are expressed in terms of normal and shear stresses on any (say ith) plane, assuming that the same characterization applies for all planes. Thus, the local components of the effective stress state σ'_i can be computed from the global effective stress vector σ' as follows:

$$\boldsymbol{\sigma}'_i = \begin{bmatrix} \sigma'_{n,i} \\ \tau_{1,i} \\ \tau_{2,i} \end{bmatrix} = (\mathbf{T}_i)^{\mathrm{T}} \boldsymbol{\sigma}' \tag{1}$$

where $\mathbf{T}_i$ represents the transformation matrix for the ith plane, which is a function of the direction cosines of the unit normal to this plane.

As there is a continuous distribution of infinite number of planes, the contribution of active planes to plastic strains is obtained through a process of numerical integration. Here, instead of monitoring all planes, a certain finite number of 'sampling planes' (also called 'integration planes') with associated weighting coefficients are used for integration. A more detailed description of integration rules is given in the following section.

As the main emphasis of this paper is on modelling of small strain stiffness based on micro-mechanical concepts, only a brief summary of the equations for yield and the plastic potential functions is given in the following for continuity and completeness.

2.3. Yield and failure functions

The yield function f_i for each integration plane can be expressed as a function of the local stresses $\sigma'_{n,i}$, $\tau_{1,i}$ and $\tau_{2,i}$ and a hardening parameter depending on a scalar measure of plastic strains $\varepsilon_i^{\mathrm{p}}$ accumulated on the respective plane

$$f_i = f_i(\sigma'_{n,i}, \tau_{1,i}, \tau_{2,i}, \varepsilon_i^{\mathrm{p}}) = 0 \tag{2}$$

Together with the plastic potential function g_i and the increment of the local plastic multiplier $\mathrm{d}\Lambda_i$, the local plastic strain contribution $\mathrm{d}\varepsilon_i^{\mathrm{p}}$ of the ith plane is given by

$$\mathrm{d}\varepsilon_i^{\mathrm{p}} = \mathrm{d}\Lambda_i \frac{\partial g_i}{\partial \sigma'_i} \tag{3}$$

To obtain the effect of $\mathrm{d}\varepsilon_i^{\mathrm{p}}$ on the global deformation behaviour, the transformation matrix $\mathbf{T}_i$ is employed again for back-transformation. Finally, the global plastic strain increment $\mathrm{d}\varepsilon^{\mathrm{p}}$ is derived

DOI: 10.1002/nag

by weighted summation over the actual number of integration planes n,

$$d\varepsilon^{p} = \sum_{i=1}^{n} d\Lambda_i \mathbf{T}_i \frac{\partial g_i}{\partial \sigma'_i} w_i \tag{4}$$

Here, w_i represents the weight factor of the ith plane associated with the employed integration rule. Bažant and Oh [14] presented symmetric integration rules with up to 2×61 planes while a decade later, Fliege and Maier [15, 16] developed an algorithm for the generation of non-symmetric integration rules of higher order incorporating optimal point locations on the unit sphere for numerical integration. Up to 900 planes allow for extremely high accuracy, but the computational effort still restricts the number of integration planes to a smaller number. In this study, the symmetric 2×33-plane integration rule according to Bažant and Oh [14, 17] is employed to balance calculation accuracy and computational effort.

Elastic strains contributing to the total strains according to the additivity postulate of the theory of plasticity (Equation (6)) can be calculated on each integration plane according to Equation (5). The same transformation matrix that is used for the transformation of plastic strains is employed to obtain the global elastic behaviour of the soil mass

$$d\varepsilon_i^{e} = \mathbf{D}_i^{e^{-1}} d\sigma'_i \tag{5}$$

In Equation (5), $\mathbf{D}_i^{e}$ represents the local elasticity matrix formulated for each integration plane

$$d\varepsilon = d\varepsilon^{e} + d\varepsilon^{p} \tag{6}$$

2.4. Constitutive relations

The yield curve of MMS depicted in Figure 1 is composed of three independent parts. The deviatoric part of the yield curve f_{dev} is defined as a straight line (Equation (7)) with an inclination of φ'_{m}. During hardening, the mobilized friction angle increases due to plastic shear strains $\varepsilon^{p}_{\gamma,\mathrm{dev}}$ accumulated on each integration plane from the deviatoric yield surface only (Equation (8)). Along this part of the yield curve non-associated flow is assumed. The mobilized dilatancy angle, ψ_{m}, which is a function of the mobilized friction angle, φ'_{m}, is used to define the direction of the plastic

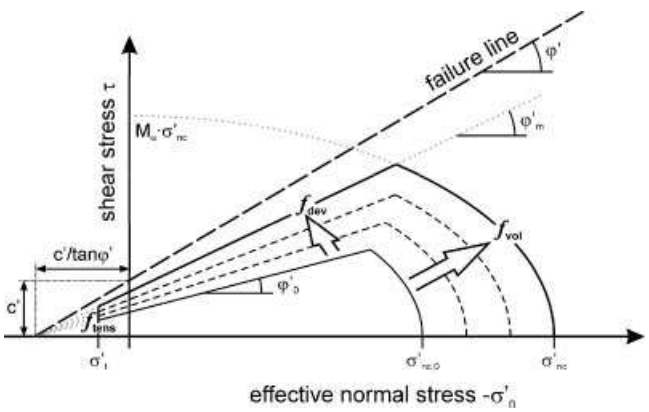

Figure 1. Yield curve and failure criterion on the integration plane level.

DOI: 10.1002/nag

strain increment calculated from the deviatoric part of the yield curve. The shape of the function depends on the peak dilatancy angle, ψ, the peak friction angle, φ' and the input parameters $\varphi'^{*}_{\mathrm{m}}$ and $\psi_{m,\min}$, which define the minimum of the mobilized dilation angle during mobilization of friction according to Scharinger and Schweiger [12]

$$f_{\mathrm{dev}} = \tau + \sigma'_{\mathrm{n}} \tan \varphi'_{\mathrm{m}} - \frac{c' \tan \varphi'_{\mathrm{m}}}{\tan \varphi'} = 0 \tag{7}$$

$$\tan \varphi'_{\mathrm{m}} = \tan \varphi'_0 + (\tan \varphi'_{\mathrm{mod}} - \tan \varphi'_0) \frac{\varepsilon^{\mathrm{p}}_{\gamma,\mathrm{dev}}}{\varepsilon^{\mathrm{p}}_{\gamma,\mathrm{dev}} + A_{\mathrm{mat}}} \tag{8}$$

$$R_{\mathrm{f}} = \frac{\tan \varphi'}{\tan \varphi'_{\mathrm{mod}}} \tag{9}$$

The failure ratio R_{f}, which is defined according to Equation (9), is employed to limit the hyperbolic curve (Equation (8)) at failure.

The second part of the yield curve f_{vol} has an elliptical shape (Equation (10)) and is conceptually similar to the one used in [1]. The shape of f_{vol} is governed by the shape factor M_α which is defined by $M_\alpha = \alpha \tan \varphi'$,

$$f_{\mathrm{vol}} = \frac{\sigma'^2_{\mathrm{n}}}{\sigma'^2_{\mathrm{nc}}} + \frac{\tau^2}{(M_\alpha \sigma'_{\mathrm{nc}})^2} - 1 = 0 \tag{10}$$

During hardening, the effective pre-consolidation stress state σ'_{nc} increases with plastic normal strains $\varepsilon^{\mathrm{p}}_{n,\mathrm{vol}}$ accumulated on this part of the yield surface (Equation (11)), whereas an associated flow rule is assumed

$$\sigma'_{\mathrm{nc}} = -[|\sigma'_{\mathrm{nc},0}|^{1-m} + (K(m-1)(p^{\mathrm{ref}})^{1-m} \varepsilon^{\mathrm{p}}_{\mathrm{n,vol}})]^{1/(1-m)} \tag{11}$$

where $\sigma'_{\mathrm{nc},0}$ denotes the initial pre-consolidation normal stress state according to the initial stress state on the respective integration plane and K is defined as a hardening parameter as follows:

$$K = \left[p^{\mathrm{ref}} \left(\frac{1}{E^{\mathrm{ref}}_{\mathrm{oed}}} - \frac{3(1-2\nu_{\mathrm{ur}})}{E^{\mathrm{ref}}_{\mathrm{ur}}} \right) \right]^{-1} \tag{12}$$

Finally, f_{tens} represents the third part of the yield curve which is defined as a tension cut-off at $\sigma'_{\mathrm{n}} = \sigma'_{\mathrm{t}}$. If no value for σ'_{t} is defined, the tensile strength on the integration plane level is related to the material shear strength according to $\sigma'_{\mathrm{t}} = c'/\tan \varphi'$. A detailed description of all constitutive relations is given in [13].

2.5. Model parameters

Most of the parameters used in the MMS for modelling strength and stiffness except for the small strain region of soil are well established and therefore they are only briefly summarized. Table I gives an overview of basic parameters and Table II summarizes the advanced parameters together with their default settings.

DOI: 10.1002/nag

Table I. Basic parameters of the multilaminate model for soil.

Symbol	Unit	Parameter
φ'	deg.	Effective friction angle
c'	kPa	Effective cohesion
ψ	deg.	Dilatancy angle
$E_{\text{oed}}^{\text{ref}}$	kPa	Reference stiffness for primary oedometer loading
A_{mat}	—	Hardening parameter for deviatoric part of yield curve
$E_{\text{ur}}^{\text{ref}}$	kPa	Elastic stiffness for unloading and reloading at reference stress
ν_{ur}	—	Poisson's ratio for unloading and reloading
p^{ref}	kPa	Reference stress
m	—	Power for stress-dependency of stiffness
$\varphi_{\text{m}}'^{*}$	deg.	Mobilized friction angle at the minimum of mobilized dilatancy
$\psi_{\text{m,min}}$	deg.	Minimum of mobilized dilatancy

Table II. Advanced parameters of the multilaminate model for soil.

Symbol	Unit	Default	Parameter
α	—	0.67	Shape parameter for vol. part of the yield curve
σ_{t}'	kPa	$c'/\tan\varphi'$	Maximum tensile strength
R_{f}	—	0.95	Failure ratio
φ_0'	deg.	1.0°	Minimum of mobilized effective friction angle
$\sigma_{\text{nc,0}}'$	kPa	−1.0	Minimum effective pre-consolidation stress state

3. DETERMINATION OF THE SMALL STRAIN MODULUS

3.1. Micromechanical concepts

Granular materials, such as soils, can be characterized as an assemblage of discrete particles and the overall behaviour of the material depends on the mechanical properties of the particle material, the packing structure and the interaction in the particle contacts. Looking at these materials from this point of view, an assembly of equally sized spheres defined by the average radius of the grains, the shear modulus, Poisson's ratio of the grain material and the inter-particle friction angle can be used to model the elastic deformational behaviour of granular soils. This assumption allows the introduction of different micromechanics-based models to determine the stress–strain behaviour at small strains and to replace approaches based on continuum mechanics theory, which are commonly used in constitutive models accounting for small strain stiffness effects.

In the past, micromechanical modelling of the stress–strain behaviour at small strains has been addressed by Duffy and Mindlin [18] and Deresiewicz [19] who proposed models for regular assemblies of elastic spheres while Digby [20], Walton [21], Chang *et al.* [22, 23] and Chang and Liao [24] presented approaches for randomly arranged granular materials. The most recent investigation of micromechanics-based models to determine the small strain modulus was presented by Yimsiri and Soga [25, 26].

In this paper, two different contact models for the estimation of small strain stiffness are examined. The basis of the first estimate is the non-linear elastic Hertz–Mindlin theory as presented

DOI: 10.1002/nag

by Mindlin and Deresiewicz [27], whereas the rough-surface contact model according to Greenwood and Tripp [28] and Johnson [29] forms the basis of the second estimate.

3.2. Packing and co-ordination number

Figure 2 shows the loosest and the densest close packing form of equally sized spheres. It is well known that the co-ordination number, i.e. the number of contacts made by a sphere with neighbouring spheres is 6 for the simple cubic packing and 12 for the hexagonal packing. For real granular material having particles of various sizes, Chang *et al.* [30] proposed the following relationship between void ratio (e), the average co-ordination number (C_n) and the mean particle size:

$$\frac{N}{V} = \frac{3C_n}{8\pi r_{grain}^3(1+e)} \tag{13}$$

where r_{grain} denotes the radius of the spherical grains, N is the total number of contacts in the volume, V. The relationship between the void ratio and the co-ordination number has been studied for different types of materials by various authors. Graton and Fraser [31] presented results of different systematic assemblies of mono-spheres as early as 1935, see Table III.

A number of experimental studies on various materials have also been conducted in the past. Smith *et al.* [32] investigated different assemblies of lead shots and found a relationship between the porosity and the co-ordination number on the basis of the assumption that an irregular and disordered packing of spherical shots can be seen as a mixture of two systematic assemblies. Field [33] studied the random assemblies of rounded stones characterized by different grain sizes, different gradings and different void ratios and Oda [34] made several investigations on various arrangements of glass balls. Very similar experiments with a rock fill material were performed by

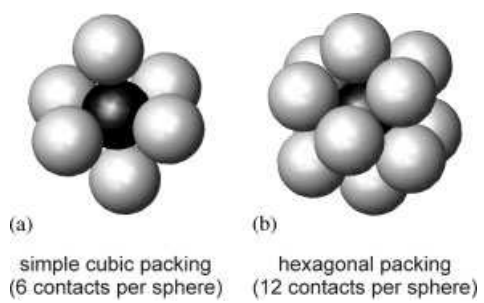

Figure 2. Different types of regularly assembled spherical grains.

Table III. Systematic arrangements of mono-spheres.

Type of packing	Void ratio e	Co-ordination number C_n
Simple cubic	0.910	6
Ortho-rhombic	0.654	8
Tetragonal	0.433	10
Rhombohedral or hexagonal	0.350	12

DOI: 10.1002/nag

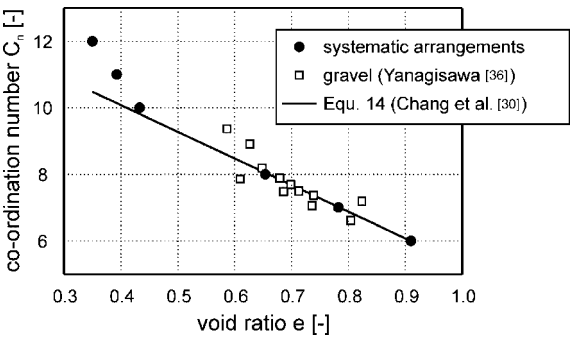

Figure 3. Relationship between C_n and e compared with experimental results for gravel.

Marsal [35] to determine another relationship. Yanagisawa [36] also presented experimental data on glass balls and gravel with two different particle shapes.

For the application within the MMS, a simple linear relation is adopted as proposed by Chang *et al.* [30]. They provide an approximation of the co-ordination number and the void ratio for the range of $0.38 \leqslant e \leqslant 0.87$ based on their studies

$$C_n = 13.28 - 8e \tag{14}$$

Figure 3 shows the experimental data of different gravels and results for systematic assemblies of equal-sized spheres together with a plot of Equation (14).

Substituting Equation (14) into Equation (13), we obtain

$$\frac{N}{V} = \frac{4.98 - 3e}{r_{\text{grain}}^3 \pi (1+e)} \tag{15}$$

3.3. Contact force

As the elastic stiffness at the small strain level is formulated as a function of the contact force in each single contact, the local stress state defined by σ'_n and τ has to be converted to the contact level for each integration plane. Yimsiri and Soga [25] proposed Equation (16) to calculate the contact force between spherical grains from the grain radius r_{grain}, the number of contacts per volume N/V and the isotropic confining pressure σ'_c,

$$f_n = \frac{3V}{2 r_{\text{grain}} N} \sigma'_c \tag{16}$$

Within their study the global stress state was transformed to the contact level, whereas in the multilaminate type of models the normal component of the stress on each integration plane can directly be substituted into Equation (16) to obtain a mathematical relationship for the normal contact force f_n between the grains and the normal stress σ'_n calculated for each individual integration plane. Substituting Equation (15) in Equation (16), we obtain

$$f_n = \frac{r_{\text{grain}}^2 \pi (1+e)}{3.32 - 2e} \sigma'_n \tag{17}$$

DOI: 10.1002/nag

A comparison of the result from Equation (17) for the cubic arrangement with the analytical result shows that exactly the same contact force is obtained with both approaches (Equation (18)). The analytical solution is calculated from the maximum number of contacts per unit area, when the corresponding grain assembly is assumed

$$f_{\mathrm{n}} = \frac{r_{\mathrm{grain}}^2 \pi (1+0.91)}{3.32-20.91} \sigma'_{\mathrm{n}} = 4 r_{\mathrm{grain}}^2 \sigma'_{\mathrm{n}} \tag{18}$$

With respect to the shear stress on the integration plane level, the tangential contact force can now be expressed as

$$f_{\mathrm{t}} = \frac{r_{\mathrm{grain}}^2 \pi (1+e)}{3.32-2e} \tau \tag{19}$$

3.4. Elastic stiffness matrix of an integration plane

Using the inter-particle contact forces f_{n} and f_{t} together with one of the contact models described later, the stiffness for each contact point K_{n} and K_{t} can be determined. Multiplying these components by the number of contacts per unit area, the local stiffness matrix for each integration plane is obtained as

$$\mathbf{K}_i^{\mathrm{e}} = \frac{3.32-2e}{r_{\mathrm{grain}}^2 \pi (1+e)} \begin{bmatrix} K_{\mathrm{n}} & 0 & 0 \\ 0 & K_{\mathrm{t}} & 0 \\ 0 & 0 & K_{\mathrm{t}} \end{bmatrix} \tag{20}$$

Considering that the soil mass consists of a set of parallel and similar planes having a spacing equivalent to the diameter of grains, the compliance matrix for a set of parallel planes can be formulated [37] as

$$\mathbf{C}_i^{\mathrm{e}} = \begin{bmatrix} C_{\mathrm{n}} & 0 & 0 \\ 0 & C_{\mathrm{t}} & 0 \\ 0 & 0 & C_{\mathrm{t}} \end{bmatrix} = \frac{1}{2 r_{\mathrm{grain}}} \mathbf{K}_i^{\mathrm{e}^{-1}} \tag{21}$$

3.5. Transformation of compliance matrix to the global level

The compliances of all sets of parallel planes that are in a local system of co-ordinates have to be transformed into a global system before they can be summed up. The procedure is similar to the one adopted for determining the elasticity matrix of a jointed rock mass [38] having a finite set of joints. Thus, the compliance matrix of the soil mass can be obtained as

$$\mathbf{C}^{\mathrm{e}} = 3 \sum_{i=1}^{n} \mathbf{T}_i \mathbf{C}_i^{\mathrm{e}} \mathbf{T}_i^{\mathrm{T}} w_i^{\ddagger} \tag{22}$$

The elasticity matrix is given by

$$\mathbf{D}^{\mathrm{e}} = (\mathbf{C}^{\mathrm{e}})^{-1} = \frac{1}{3} \left(\sum_{i=1}^{n} \mathbf{T}_i \mathbf{C}_i^{\mathrm{e}} \mathbf{T}_i^{\mathrm{T}} w_i \right)^{-1} {}^{\ddagger} \tag{23}$$

‡As integration over the surface of a unit sphere is performed instead of integration over the volume of a unit sphere when weighted summation according to one of the discussed integration rules is employed, a factor of 3 has to be applied to obtain the global compliance matrix.

DOI: 10.1002/nag

3.6. Hertz–Mindlin contact model

We now consider the non-linear elastic Hertz–Mindlin contact model to characterize the contact between elastic perfectly rounded spheres with smooth surfaces. In such cases where the Hertzian theory is applicable, it predicts a plane, circular contact surface of radius a_0 as

$$a_0 = \left[\frac{3(1-\nu_{\text{grain}})}{8G_{\text{grain}}} r_{\text{grain}} f_{\text{n}} \right]^{1/3} \tag{24}$$

where G_{grain} and ν_{grain} denote the shear modulus and Poisson's ratio of the grain material. The size of the spherical grains is defined by the grain radius r_{grain}.

Figure 4 shows the deformation w_0 and the radius a_0 of the contact zone of two spherical grains subjected to an applied normal force f_{n}. The following equation gives a theoretical expression for w_0:

$$w_0 = 2 \left[\frac{3 f_{\text{n}}(1-\nu_{\text{grain}})}{8G_{\text{grain}} r_{\text{grain}}^{1/2}} \right]^{2/3} = \frac{2a_0^2}{r_{\text{grain}}} \tag{25}$$

Hence, the contact stiffness in the direction normal to the contact surface K_{n} is given as [27]

$$K_{\text{n}} = \left(2 \frac{\partial w_0}{\partial f_{\text{n}}} \right)^{-1} = \left[\frac{3 r_{\text{grain}} G_{\text{grain}}^2}{(1-\nu_{\text{grain}})^2} f_{\text{n}} \right]^{1/3} \tag{26}$$

The tangential component of the contact stiffness formulated by Bowden and Tabor [39] and Johnson [29] is

$$K_{\text{t}} = \frac{2(1-\nu_{\text{grain}})}{(2-\nu_{\text{grain}})} \left(1 - \frac{f_{\text{t}}}{f_{\text{n}} \tan \varphi_{\text{int}}} \right)^{1/3} K_{\text{n}} \tag{27}$$

where f_{t} denotes the tangential force at the contact of two particles.

The relationship between K_{n}, K_{t}, f_{n} and f_{t} (Equations (26) and (27)) is shown in Figure 5 for the set of parameters listed in Table IV, which correspond to the average values of medium-grained sand. It is seen that K_{n} and K_{t} obtained from the Hertz–Mindlin contact model are non-linear

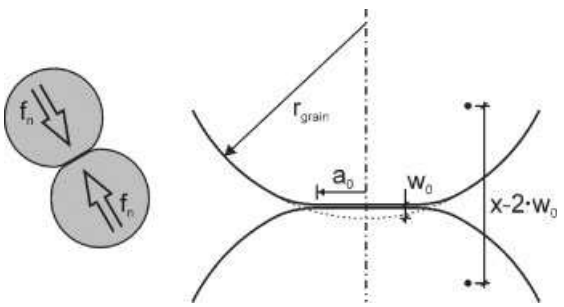

Figure 4. Deformation of two grains in contact according to the Hertzian contact theory.

DOI: 10.1002/nag

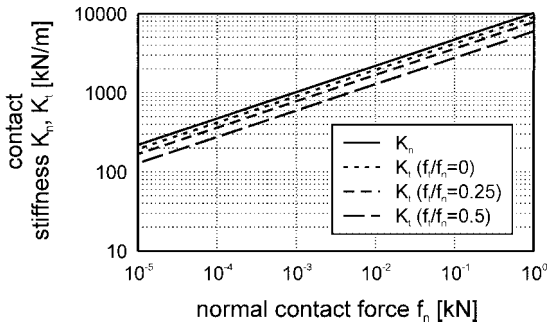

Figure 5. Normal stiffness K_n and tangential stiffness K_t *vs* normal force f_n in one contact (log scale).

Table IV. Input parameters for medium sand (Hertz–Mindlin contact model).

Parameter		Value	Unit
Shear modulus of the grain material	G_{grain}	30	GPa
Poisson's ratio of the grain material	v_{grain}	0.2	—
Average grain radius	r_{grain}	0.25	mm
Inter-particle friction angle	φ_{int}	35	deg.

functions of f_n and f_t, which vary with the local stress state on each particular integration plane. It is noted that the pressure dependency of the contact stiffness predicted by the Hertz–Mindlin contact model is fixed with the power of $\frac{1}{3}$, whereas values in the range of 0.5–0.75 are presented by many authors [40–42] based on experimental studies for granular materials.

3.7. Rough-surface contact model

To obtain a deeper insight into small strain stiffness behaviour of soil masses, a model with rough spherical particles is now investigated. Greenwood and Tripp [28] assumed that the surface of a rough particle can be described as an assembly of spherical asperities with equal radii. A Gaussian or normal probability density function is employed to characterize the distribution of the asperity heights. The main conclusion of their work is that the classical Hertzian solution provides the upper load limit for a rough surface and that at lower load levels significant differences occur. Figure 6 compares the pressure distribution over the contact area for different load levels.

As expected, the radius of the contact area a^{rough} is much larger at low loads and the maximum contact pressure $p^{rough}(0)$ between rough surfaces is much lower. Greenwood and Tripp [28] defined the effective contact radius by

$$a^{rough} = \frac{3\pi \int_0^\infty \rho p^{rough}(\rho) \partial\rho}{4 \int_0^\infty p^{rough}(\rho) \partial\rho} \tag{28}$$

where ρ is the radial distance from the centre of the contact area and $p^{rough}(\rho)$ is the pressure distribution function.

DOI: 10.1002/nag

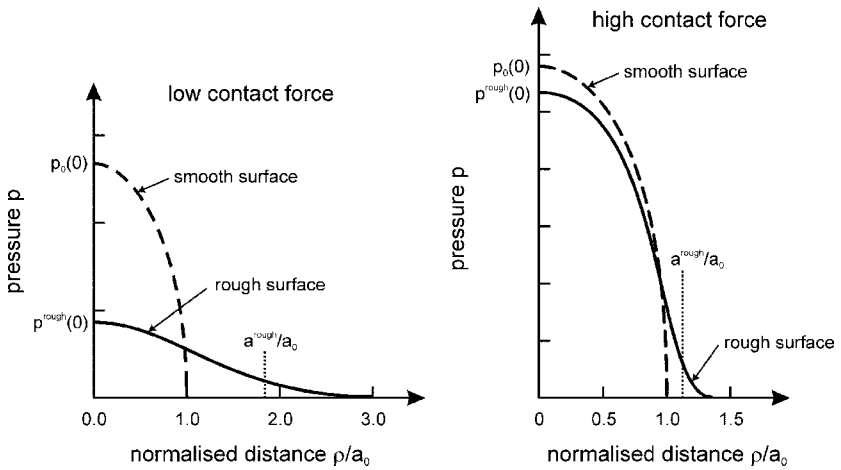

Figure 6. Comparison of effective pressure distribution of rough-surface contact model and the Hertzian theory [28].

To obtain a solution for the contact stiffness similar to Equation (26), Johnson [29] used two independent non-dimensional parameters. The first parameter, denoted as α^{rough}, can be expressed by

$$\alpha^{\text{rough}} = \frac{2\sigma_s}{2w_0} = \frac{\sigma_s r_{\text{grain}}}{a_0^2} = 4\sigma_s \left(\frac{r_{\text{grain}} G_{\text{grain}}^2}{9(1-\nu_{\text{grain}})^2 f_n^2} \right)^{1/3} \tag{29}$$

where w_0 is the bulk compression of one sphere as defined previously and a_0 represents the radius of the contact area given by the Hertz theory. The standard deviation of the distribution of the asperity heights σ_s is an additional input parameter to describe the roughness of the particle surface, whereas the mean value of the height distribution is not considered in this approach. The numerator and denominator from the original equation for parameter α^{rough}, which depends on the normal contact force f_n, are multiplied by a factor of 2, because this study considers the contact of two spheres with rough surfaces whereas the original investigation considered the contact between a rough sphere and a rigid, smooth plane.

The second parameter used by Greenwood and Tripp [28] to describe the mechanical properties of rough surfaces is

$$\mu = \frac{8}{3}\eta_s \sigma_s \left(\frac{2r_{\text{grain}}}{\kappa_s} \right)^{1/2} \tag{30}$$

where the parameter μ depends on the topography of the surface but not on the load. In the above equation η_s is the asperity density and κ_s denotes the asperity summit radius.

Figure 7 shows the results of experimental investigations presented by Johnson [29] for different values of μ, whereas the influence of the surface roughness on the ratio of effective contact radius a^{rough} and the Hertzian radius a_0 can be seen. Comparison of experimental results for different values of μ when plotting parameter α^{rough} with the maximum contact pressure $p^{\text{rough}}(0)$ normalized by the corresponding magnitude $p_0(0)$ obtained from the Hertzian theory is given in Figure 8. Both diagrams lead to the conclusion that the radius ratio a^{rough}/a_0 is primarily a function of α^{rough}

DOI: 10.1002/nag

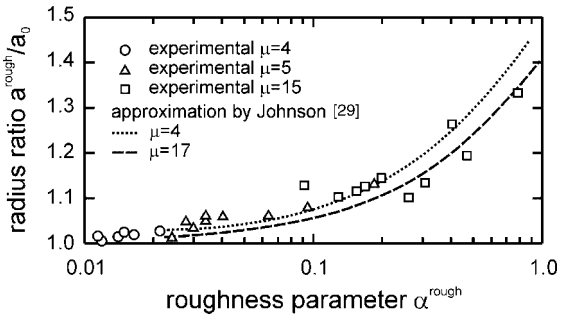

Figure 7. Influence of the surface roughness on the effective contact radius a^{rough} compared with the radius a_0 calculated from the Hertzian theory [29].

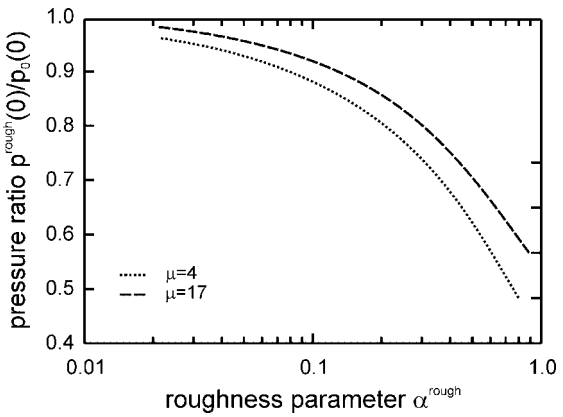

Figure 8. Influence of the surface roughness on the maximum contact pressure $p^{\text{rough}}(0)$ compared with the maximum pressure $p_0(0)$ calculated from the Hertzian theory [29].

and the parameter μ has a secondary effect on the result. Hence, it is assumed in this study that the ratio a^{rough}/a_0 depends on parameter α^{rough} only. A plot of the best-fit curve (Equation (31)) for the data presented by Johnson [29] is shown in Figure 9 and can be expressed as

$$\frac{a^{\text{rough}}}{a_0} = \frac{5(20+7\alpha^{\text{rough}^{0.5}})}{100+\alpha^{\text{rough}^{0.5}}} \tag{31}$$

The normal contact stiffness K_{n} can now be calculated based on the Hertzian contact theory by using a^{rough} instead of a_0,

$$w^{\text{rough}} = \frac{2a^{\text{rough}^2}}{r_{\text{grain}}} \tag{32}$$

$$K_{\text{n}}^{\text{rough}} = \left(2\frac{\partial w^{\text{rough}}}{\partial f_{\text{n}}}\right)^{-1} \tag{33}$$

DOI: 10.1002/nag

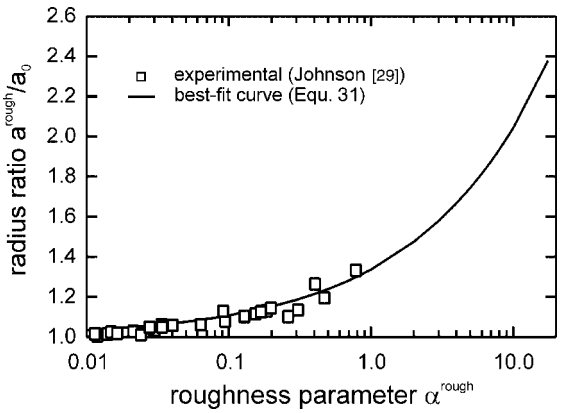

Figure 9. Relationship between the roughness parameter α^{rough} and the radius ratio a^{rough}/a_0 (Equation (31)).

Table V. Input parameters for medium sand (rough-surface contact model).

Parameter		Value	Unit
Shear modulus of the grain material	G_{grain}	30	GPa
Poisson's ratio of the grain material	ν_{grain}	0.2	—
Average grain radius	r_{grain}	0.25	mm
Inter-particle friction angle	φ_{int}	35	deg.
Standard deviation of asperity heights	σ_{s}	5×10^{-6}	m

The tangential component of the contact stiffness $K_{\text{t}}^{\text{rough}}$ is formulated according to Equation (27), whereas K_{n} is substituted by the corresponding value from the rough-surface contact model $K_{\text{n}}^{\text{rough}}$. This decrease in the tangential contact stiffness with the normal contact stiffness is in accordance with the findings of Johnson [29] for rough surfaces

$$K_{\text{t}}^{\text{rough}} = \frac{2(1-\nu_{\text{grain}})}{(2-\nu_{\text{grain}})}\left(1-\frac{f_{\text{t}}}{f_{\text{n}}\tan\varphi_{\text{int}}}\right)^{1/3} K_{\text{n}}^{\text{rough}} \tag{34}$$

Using the parameters for the medium sand described previously, extended by the standard deviation of the distribution of asperity heights σ_{s} (Table V), the relationship between $K_{\text{n}}^{\text{rough}}$, $K_{\text{t}}^{\text{rough}}$, f_{n} and f_{t} can be calculated from Equations (33) and (34).

A comparison of results obtained with the Hertz–Mindlin contact model and those obtained with the rough-surface contact model is given in Figure 10. It can be clearly seen that the graphs of $\log K_{\text{n}}^{\text{rough}}$ and $\log K_{\text{t}}^{\text{rough}}$ against $\log f_{\text{n}}$ approach the result for smooth surfaces at high contact forces but show significant differences when lower values of f_{n} are considered. Together with the decrease in the absolute values a significant increase in the slope of the graphs is found. The difference in stress dependency of the small strain modulus on hydrostatic stress predicted by the Hertz–Mindlin contact model compared with the experimental findings for various materials was pointed out by many authors [22, 25, 41, 43]. For example, Janbu [40], Goddard [41], von Soos

DOI: 10.1002/nag

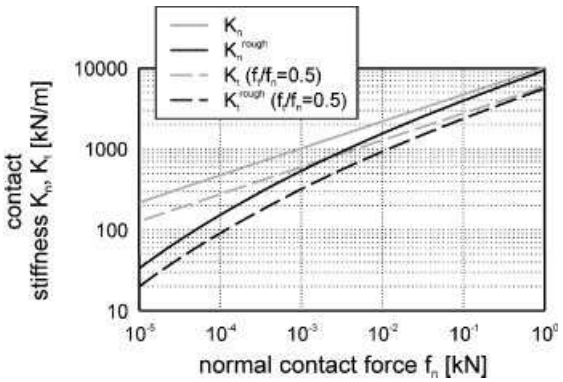

Figure 10. Normal stiffness $K_{\mathrm{n}}^{\mathrm{rough}}$ and tangential stiffness $K_{\mathrm{t}}^{\mathrm{rough}}$ *vs* normal force f_{n} in one contact (log scale).

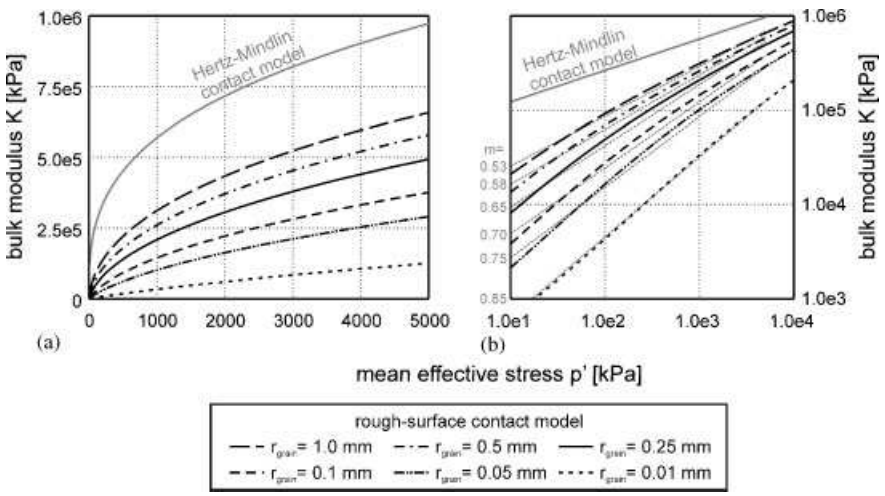

Figure 11. Bulk modulus K on the global level *vs* mean effective stress p' from the rough-surface contact model: (a) variation of the average grain radius and (b) log-scale.

and Bohac [42] and Lade and Abelev [44] presented values of the exponent m dependent on the type of the investigated material. Sandy soils are found in the range of $0.5 \leqslant m \leqslant 0.75$ whereas the stiffness of finer materials tends to increase with the applied stress according to a power of up to 1.0.

Approximately this variation of the exponent m, which is an outcome of the analysis with the rough-surface contact model, is observed in Figure 11(b) where the results from the rough-surface contact model with varying grain sizes are plotted in double logarithmic scale from numerical simulations of isotropic compression tests.

Up to a mean effective stress of 5000 kPa, very good accordance with the experimental data is achieved employing the micromechanics-based approach for rough-surface spheres. Coarse materials show an increase in the stiffness with the power of 0.5 whereas a steeper slope is found

DOI: 10.1002/nag

Table VI. Pressure dependency of stiffness at small strains predicted by the rough-surface contact model for different average grain sizes.

		Power m	
Material	Average grain diameter (mm)	Rough-surface contact model	von Soos Bohac [42]
Coarse sand	2.0	0.53	0.55–0.70
Coarse sand	1.0	0.58	
Medium sand	0.5	0.65	
Fine sand	0.2	0.70	0.60–0.75
Fine sand	0.1	0.75	
Silt	0.02	0.85	0.70–0.90

for finer materials. Table VI summarizes the results from the numerical analysis in comparison with values presented in the literature for the corresponding materials.

Despite the fact that the presented rough-surface approach is developed for granular materials and that most of the assumptions regarding the grain shape and contact conditions will not hold for e.g. silty soils, the prediction of the stress dependency of the stiffness for these materials is very satisfactory.

4. ELASTIC STIFFNESS IN THE SMALL STRAIN RANGE

This section deals with two basic features of soil behaviour, namely the monotonic decay of stiffness during shearing and the increase when the direction of the stress path changes. The first one is depicted in Figure 12 where the typical S-shaped distribution of the stiffness over strains during shearing can be seen. After the approximately linear plateau at very small strains, which is associated with linear elastic material behaviour, the stiffness decreases monotonically with the accumulation of shear strains. Atkinson and Sallfors [45] reported values between 0.001 and 0.01% of shear strain for the onset of the stiffness decay dependent on the soil type. Beyond approximately 1% of shear strain, plastic behaviour dominates.

The second issue that has to be addressed when the stiffness at small strains is considered is the loading history. A deviation from the previous loading direction results in an increase in soil stiffness, whereas a full load reversal yields the stiffest material response.

4.1. Stiffness degradation

In the MMS the strain-dependent stiffness decay is modelled directly by fitting laboratory test data with mathematical functions of the applied strain. The general shape of these curves discussed before has been presented by many authors, e.g. [46–48]. Very similar to the function presented by Santos and Gomes Correia [49] for the decrease in the shear modulus with accumulated shear strain is the one derived by Soga *et al.* [50]. Equation (35) shows their mathematical formulation of the empirical expression for a stiffness degradation curve with a small number of additional parameters

$$\frac{G}{G_{\max}} = \frac{1}{1 + a_{\deg} \gamma^{b_{\deg}}} \tag{35}$$

DOI: 10.1002/nag

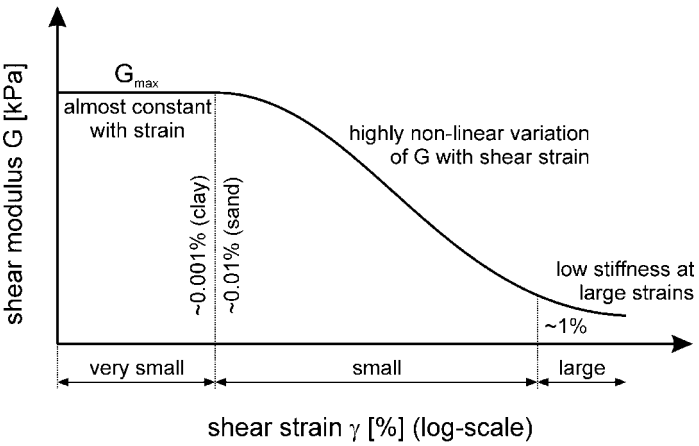

Figure 12. Variation of stiffness with strain at the small strain level.

The material constants a_{deg} and b_{deg} control the shape of the normalized degradation curve. The value of a_{deg} influences the strain level at which the stiffness begins to degrade, whereas the normalized degradation curve changes its gradient with b_{deg}.

Within the MMS employing one of the discussed approaches to determine the stiffness at very small strains, its reduction during shearing is governed by the change in the accumulated shear strain γ_i on each of the integration planes. Particularly, the two components of the contact stiffness K_{n} and K_{t} decay during shearing and therefore influence the global stiffness degradation curve. As K_{t} is dependent on K_{n}, the degradation of both components of the contact stiffness follows the same curve (Figure 13). Hence, this approach is comparable with formulations where the shear modulus is reduced with the accumulation of shear strains, whereas the relationship between the shear modulus and the bulk modulus is governed by the Poisson ratio. It should be noted that the following equation holds for integration planes and therefore on global-level Poisson's ratio may change due to different mobilizations of shear strains on individual planes

$$\frac{K_{\mathrm{n}}}{K_{\mathrm{n,max}}} = \frac{K_{\mathrm{t}}}{K_{\mathrm{t,max}}} = \frac{1}{1 + a_{\mathrm{deg}} \gamma_i^{\,b_{\mathrm{deg}}}} \tag{36}$$

Thus, the two parameters, a_{deg} and b_{deg}, qualitatively affect the stiffness degradation curve in the same manner as proposed by Soga *et al.* [50] but their magnitude changes if used on integration plane level.

The minimum value of the contact stiffness is not defined by the employed degradation curve. If the accumulated shear strain γ_i on the integration plane level exceeds the magnitude where the contact stiffness associated with the elastic unloading/reloading stiffness $E_{\mathrm{ur}}^{\mathrm{ref}}$ obtained from conventional tests gets larger than the one resulting from the micromechanics-based approach, deformation behaviour is modelled exclusively with the constitutive relations implemented for large strains. Generally, this transition from the small strain to the large strain region takes place on each integration plane at a different state of global deformation which turns the sharp bend in Figure 13 into a smooth transition at the global level (Figure 14). Comparing the degradation curve defined by Equation (36) on the integration plane level (Figure 13) with the resulting degradation curve on

DOI: 10.1002/nag

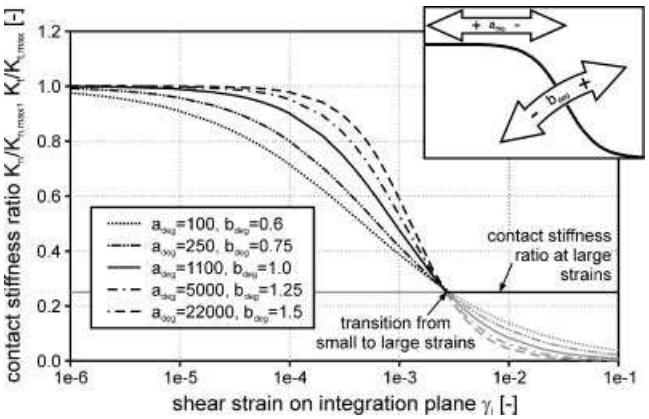

Figure 13. Influence of a_{deg} and b_{deg} on the stiffness degradation curve on the integration plane level.

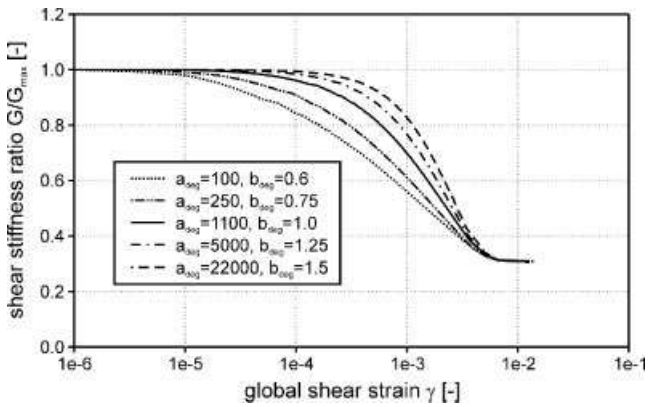

Figure 14. Typical plot of the global stiffness degradation at the small strain level obtained with MMS for different sets of a_{deg} and b_{deg}.

the global level due to triaxial compression (Figure 14), it can be clearly seen that all tendencies are the same but small differences emerge. As shear strains develop independently on different integration planes, different states of the contact stiffness ratio $K_{\mathrm{n}}/K_{\mathrm{n,max}} = K_{\mathrm{t}}/K_{\mathrm{t,max}}$ on different integration planes apply for a single point on the global stiffness degradation curve. Therefore, the onset of degradation on the global level occurs at slightly higher shear strain compared with the magnitude of the corresponding value on the integration plane level. Another special characteristic arises in loading cases where the direction of principal stresses is perpendicular to one or more integration planes, e.g. triaxial, biaxial and oedometer tests. In these cases no shearing occurs on these planes and therefore no degradation of stiffness is taken into account for the calculation of the global stiffness matrix. Hence, the stiffness on the global level is influenced by small strain stiffness on some planes all the time and does not completely reduce to the input value for the stiffness at large strains. To find the best-fit curve for materials tested in laboratory, different combinations of a_{deg} and b_{deg} have to be analysed.

DOI: 10.1002/nag

4.2. Loading history

To include the dependency of the elastic material stiffness on the loading direction in the proposed approach, the material's strain history is recorded. In MMS, the elastic stiffness matrix is determined from the contributions of all integration planes which means that data for all integration planes have to be stored. To determine the elastic stiffness on each contact plane due to changes in the direction of the shear strain increment, the relationship between the angular change in direction δ and the corresponding stiffness increase has to be defined. Richardson [51] presented a large number of triaxial tests performed with respect to the material stiffness at small strains and the effect of changes in the loading direction. Although all laboratory test results only provide information on the dependency of the material stiffness increase due to changes in the loading direction on the global level, a similar correlation between these values is used on the integration plane level in MMS. By fitting the experimental data with a continuous function, the two components of the contact stiffness, K_n and K_t, are directly related to the angular change δ of the shear strain increment on the respective integration plane. As minor deviations of the strain path direction do not cause a significant change in stiffness, the linearization according to the dashed line in Figure 15 was implemented, i.e. only values of $\delta > 45°$ produce an increase in the elastic stiffness at small strains on the integration plane level. Considering various stress paths starting at the same point in general stress space, only two directions defined by the direction change ω are unique. $\omega = 0°$ (continuous loading) and $\omega = 180°$ (full stress reversal) represent these two directions as the angle ω is defined in p'–q space. Hence, all other values of ω can apply for an infinite number of stress paths activating different integration planes in a multilaminate model. Figure 16 illustrates the model response for stress paths starting at K_0-conditions and heading towards different directions. It can be clearly seen that the maximum stiffness at load reversals and the constant stiffness for low values of ω are predicted accurately whereas the results between these two boundaries scatter around the intended curve. This effect is related to the limited number of integration planes used in a multilaminate model. Owing to the direction of the stress path, different integration planes contribute to the global result and therefore influence it in a different way. Only an increase

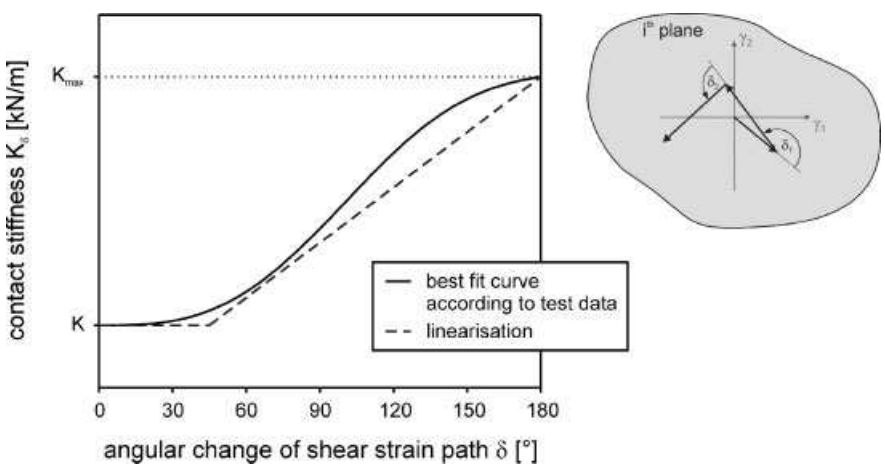

Figure 15. Dependency of the contact stiffnesses K_n and K_t on the angular change of the shear strain increment δ on the integration plane level.

DOI: 10.1002/nag

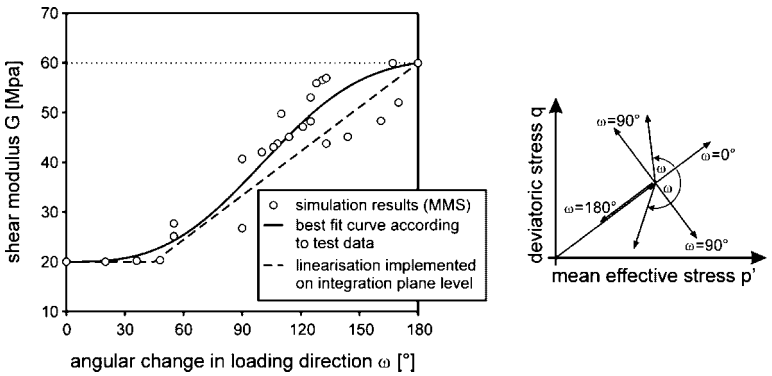

Figure 16. Effect of varying stress path directions on global shear stiffness G predicted by the multilaminate model for soil.

to hundreds of integration planes would reduce the variation in the predicted stiffness from the proposed curve. However, this scatter is not significant from a practical point of view.

5. DRAINED TRIAXIAL COMPRESSION TESTS

To show the performance of MMS when it is employed for the numerical simulation of element tests, laboratory data from drained triaxial tests presented by Kohata *et al.* [52] are compared with simulation results in this section. As the main focus of the experimental investigations was on the deformation behaviour at small strains, results obtained with the proposed model in this strain range are highlighted in the following. Table VII summarizes the strength and stiffness parameters for medium-dense Hostun sand. Input parameters for the rough-surface contact model, which is employed for the calculation of the elastic stiffness in the small strain range are given in Table VIII.

The co-ordination number used in the calculation was derived from the initial void ratio $e_0 = 0.76$ ($D_r = 0.65$) employing Equation (14) and the average grain radius is chosen according to the grain size distribution presented by Desrues *et al.* [53] for Hostun sand. As it is assumed that mechanical properties of the grain material are associated with those of the parent intact rock, values for G_{grain}, ν_{grain} and φ_{int} are chosen according to the comprehensive database on the mechanical properties of rocks presented by Lama and Vutukuri [54]. The standard deviation of asperity heights was estimated with reference to Yimsiri and Soga [25]. The shape of the stiffness degradation curve at small strains is governed by a_{deg} and b_{deg}, which are taken to match the typical stiffness degradation of sand.

Experimental data used for comparison is obtained from the drained triaxial compression tests with isotropic consolidation. The cell pressure is increased to 78.4 kPa during consolidation and kept constant during shearing of the specimen. Figure 17 shows the stress–strain behaviour observed in the laboratory and results obtained with MMS considering the input parameters discussed previously. In order to point out the deformation behaviour in the small strain range, the first part of the curve (Figure 17) is illustrated in more detail by using different scales (Figures 18 and 19). The very first part of the stress–strain curve ($\varepsilon_a \leqslant 0.01\%$) depicted in Figure 18 shows the almost linear elastic material behaviour according to the stiffness at very small strains $G_{\max}$. The following

DOI: 10.1002/nag

Table VII. Strength and stiffness parameters for the Hostun sand.

Parameter	Symbol	Unit	Value
Effective friction angle	φ'	deg.	39
Effective cohesion	c'	kPa	0
Dilatancy angle	ψ	deg.	0
Reference stiffness for primary oedometer loading*	E_{oed}^{ref}	kPa	10 000
Reference stiffness for unloading and reloading*	E_{ur}^{ref}	kPa	25 000
Deviatoric hardening parameter	A_{mat}	—	0.008
Poisson's ratio for unloading and reloading	ν_{ur}	—	0.20
Reference stress	p^{ref}	kPa	100
Power for stress dependency of stiffness	m	—	0.65
Shape parameter for the volumetric part of the yield curve f_{vol}	α	—	0.67
Mobilized friction angle at the minimum of mobilized dilatancy	$\varphi_m'^*$	deg.	10
Minimum of mobilized dilatancy	$\psi_{m,min}$	deg.	−5

*Based on the typical ratio between E_0^{ref}, E_{ur}^{ref} and E_{oed}^{ref}.

Table VIII. Small strain stiffness parameters for the Hostun sand.

Parameter	Symbol	Unit	Value
Shear modulus of the grain material	G_{grain}	GPa	30
Poisson's ratio of the grain material	ν_{grain}	—	0.2
Average grain radius	r_{grain}	mm	0.2
Inter-particle friction angle	φ_{int}	deg.	40
Standard deviation of asperity heights	σ_s	m	3.5e−6
Co-ordination number	C_n	—	7.2
Definition of the degradation curve	a_{deg}	—	475
Definition of the degradation curve	b_{deg}	—	0.85
Stiffness ratio for the modification of hardening	f_{hard}	—	0.0

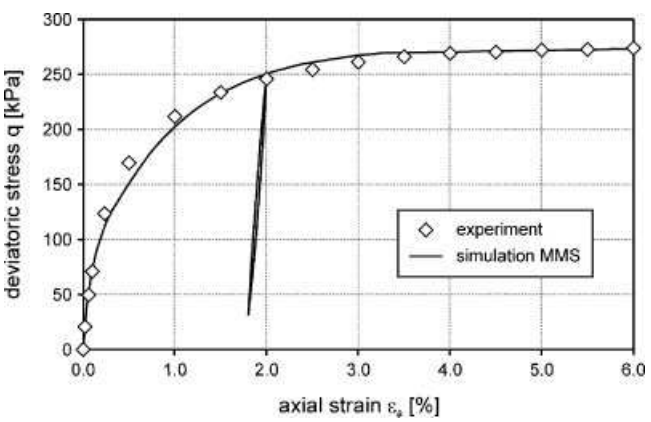

Figure 17. Stress–strain curve of the Hostun sand in drained triaxial compression.

DOI: 10.1002/nag

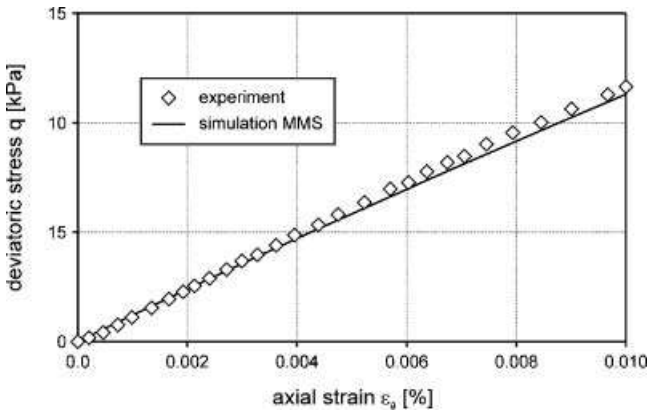

Figure 18. Very first part of the stress–strain curve from triaxial compression tests on the Hostun sand ($0\% \leqslant \varepsilon_a \leqslant 0.01\%$).

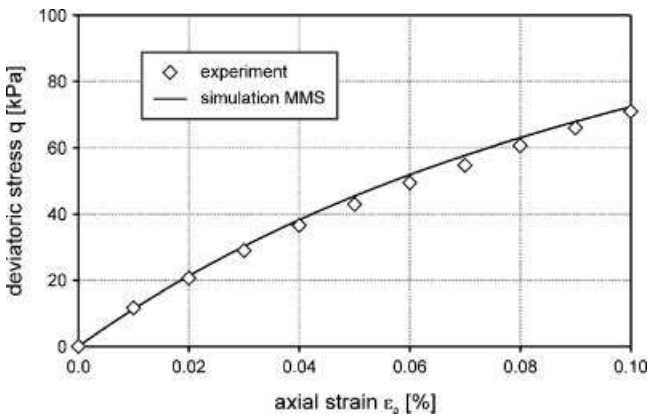

Figure 19. Stress–strain curve from triaxial compression tests on the Hostun sand in the range of $0\% \leqslant \varepsilon_a \leqslant 0.1\%$.

part, up to an axial strain of 0.1% (Figure 19), shows distinct non-linearity due to the degradation of elastic stiffness and increasing plasticity. Outside the small strain region, where volumetric and deviatoric hardening govern the deformation behaviour, non-linearity of the stress–strain curve increases until failure is reached at the maximum deviatoric stress $q_{\max} \approx 273\,\text{kPa}$. It can be clearly seen from Figures 17 to 19 that very good accordance with experimental data is achieved over the entire strain range.

6. NUMERICAL SIMULATION OF A DEEP EXCAVATION

Predictive capabilities of the constitutive model discussed before are evaluated by means of a deep excavation problem in this section. In order to point out the performance of the MMS with small strain stiffness in comparison with the model without, a simplified example has been chosen.

DOI: 10.1002/nag

6.1. *Specification*

The geometry used for this example including all dimensions and boundary conditions is shown in Figure 20 together with the finite element mesh. It consists of approximately 270 15-noded triangular elements with about 2360 nodes and 3260 stress points. The final depth of 12 m is simulated in three steps of 4 m excavation each. The total width of the pit is 30 m. The support system consists of a diaphragm wall with a thickness of 80 cm and two layers of steel struts, the first one at −3 m and the second one at −7 m below the surface level. The wall is modelled as a beam with linear elastic material behaviour. Owing to the fact that only the serviceability limit state is analysed in the following, reduction of stiffness according to cracks in the concrete structure is not taken into account. The struts are modelled as fixed-end anchors with an equivalent length of 15 m which is half of the width of the excavation pit. Linear elastic material behaviour is assumed for the struts. Values to be applied for the wall and the struts are summarized in Table IX. For all calculations with the MMS, homogeneous subsoil conditions are assumed. Material properties that correspond to the medium-dense Hostun sand were discussed in the previous section (Tables VII and VIII). In all simulations, interface elements with a Mohr–Coulomb criterion are used at both sides of the wall to model the interaction between soil and wall assuming the wall friction being 0.7 times the strength of the soil.

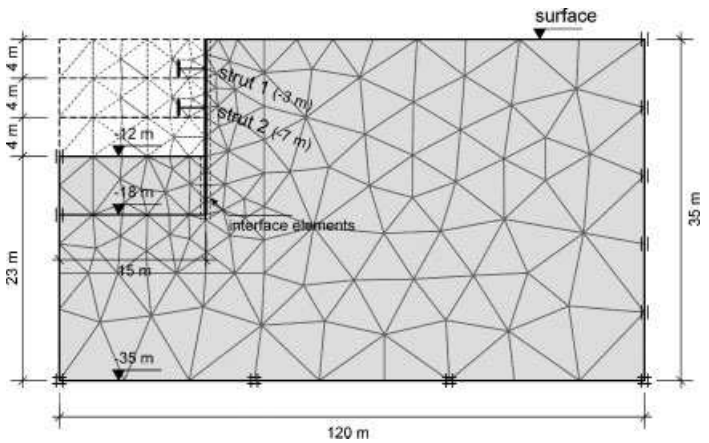

Figure 20. Geometry of the numerical model and finite element mesh.

Table IX. Properties of retaining structure.

Parameter		Unit	Diaphragm wall	Struts
Flexural rigidity	EI	$kN\,m^2/m$	1.28e6	—
Axial stiffness	EA	kN/m	2.40e7	5.25e5
Poisson's ratio	ν	—	0.15	—
Specific weight	w	kN/m/m	12.0	—
Plastic bending moment	M_p	kN m/m	—	—
Plastic axial force	N_p	kN/m	—	—

DOI: 10.1002/nag

6.2. Calculation steps

After the specification of the initial conditions according to $\sigma'_v = \gamma^* h$ and $\sigma'_h = K_0^* \gamma^* h$, where h is the depth below the surface and K_0 the lateral earth pressure coefficient at rest, the following six construction phases have been defined:

- Installation of the retaining wall (wished in place).
- First excavation step to a depth of 4 m below the surface level.
- Installation of the upper level of struts at −3 m below the surface level.
- Second excavation step to a depth of 8 m below the surface level.
- Installation of the lower level of struts at −7 m below the surface level.
- Third excavation step to a depth of 12 m below the surface level.

6.3. Comparison of results

In this section, results obtained with different versions of MMS, with (MMS_{sss}) and without (MMS) consideration of small strain stiffness, are compared. The evolution of horizontal displacements of the wall during excavation obtained with the MMS is depicted in Figure 21. Comparing Figure 21(a) and (b), the influence of small strain stiffness on the results can be clearly seen. Especially in the first excavation step, deformations obtained with the model incorporating small strain stiffness are much smaller than the corresponding values from the same constitutive model determined without consideration of small strain stiffness effects. Because of the degradation in stiffness in the small strain model, this tendency reduces during further excavation. In the final excavation step from −8 to −12 m, additional deformations obtained with the two models are very similar in the upper part (0–9 m) but still differ along the embedded length. The base of the wall shows small horizontal

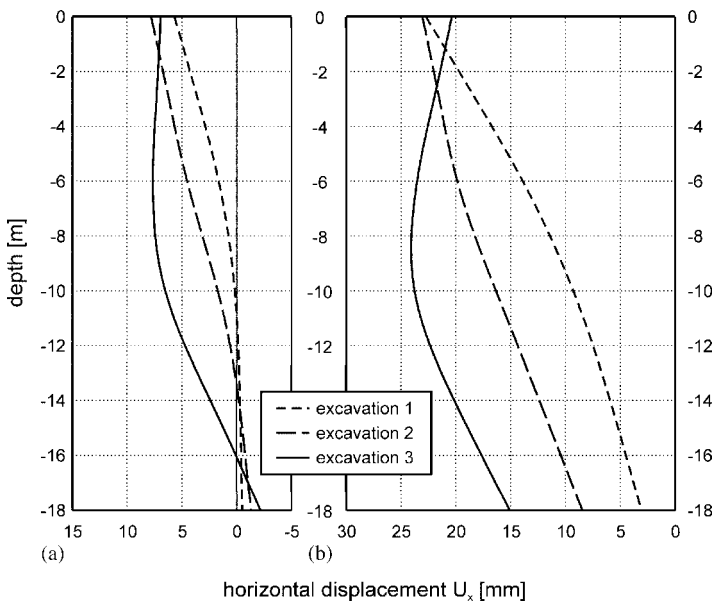

Figure 21. Evolution of horizontal wall displacements during excavation: (a) MMS_{sss} and (b) MMS.

DOI: 10.1002/nag

displacement towards the soil when analysed with the small strain model. This tendency is not entirely realistic, but is considered negligible due to its low magnitude and could be avoided by a small modification of input parameters.

The top of the wall is subjected to the maximum displacement during the first calculation steps and significant rotation of the upper part of the structure occurs. The model without consideration of small strain stiffness effects actually predicts the rotation of the entire wall towards the pit from the beginning of the excavation. With ongoing construction and installation of the struts this rotation reduces and changes direction in the end. Maximum displacements develop at -9 m below the surface during the final excavation step.

The distributions of bending moments for the two simulations are depicted in Figure 22. In the upper part, the shape of the curves is very similar while differences in the maximum value and along the embedded length are obtained. The model without small strain stiffness results in a maximum bending moment of $M \approx 381$ kN m/m, whereas the small strain model gives a maximum value of $M \approx 301$ kN m/m. Examining the distributions of bending moments from -12 to -18 m, the model without small strain stiffness indicates free earth support of the wall, whereas the model incorporation small strain stiffness tend towards a fixed earth support. This effect is due to the differences in the relative stiffness of the diaphragm wall and soil which changes according to the varying response from the constitutive models employed. Figure 23 shows the comparison of strut forces after the final excavation phase.

Beside deformations and internal forces of structural elements, settlements outside the excavation pit and vertical displacements across its base are of interest in most cases. Comparison of the results from the two models employed for this study is made in Figures 24 and 25. It can be observed that for the model without small strain stiffness, 5 mm of settlement is calculated at the

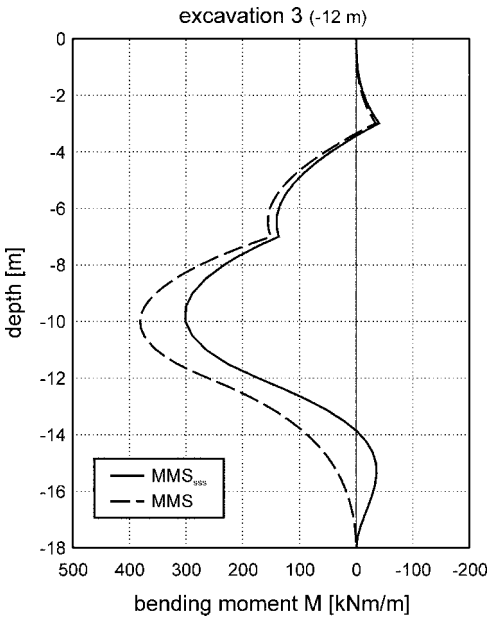

Figure 22. Distribution of bending moments obtained with different models (MMS_{sss} and MMS).

DOI: 10.1002/nag

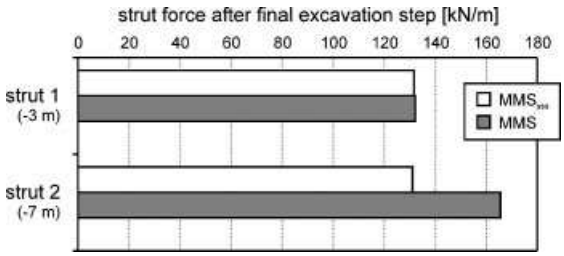

Figure 23. Strut forces after final excavation phase obtained with different models (MMS_{sss} and MMS).

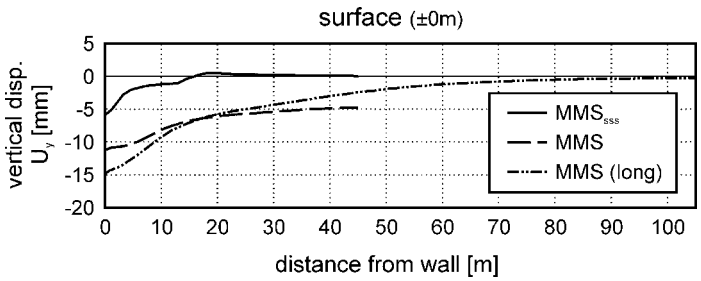

Figure 24. Vertical displacements of the surface next to the excavation obtained with different constitutive models (MMS_{sss} and MMS).

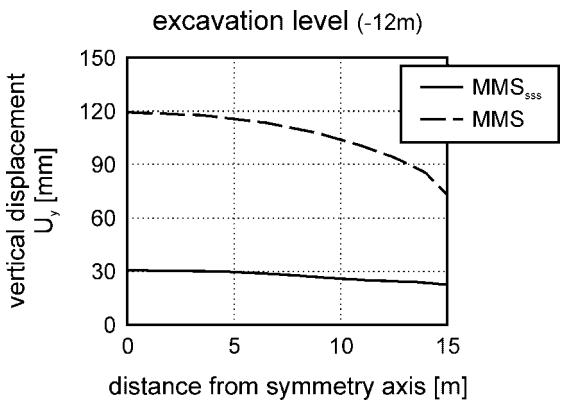

Figure 25. Vertical displacements of the base of the excavation obtained with different constitutive models (MMS_{sss} and MMS).

boundary of the mesh indicating that the model boundaries are not at a sufficient distance from the excavation. Therefore, an additional analysis has been performed with an extended mesh, referred to as MSS (long). Results obtained with both numerical models are shown in Figure 24. As the influence of the model dimensions is restricted to the settlement trough predicted by the MMS without small strain stiffness exclusively, the enlarged mesh was used for this simulation only.

DOI: 10.1002/nag

It can be clearly seen that the settlement trough predicted by the MMS is strongly influenced by the small strain stiffness. With small strain stiffness included, a much narrower trough is obtained and the maximum settlement is in the range of 50% of the value predicted by the basic version of the model. It is emphasized that reliable settlements can usually not be achieved with simple elastic–perfectly plastic constitutive models (e.g. Mohr–Coulomb model).

As most stress points below the base of the excavation pit are in unloading during excavation, vertical movement of the base of the excavation (-12 m) depends mainly on the elastic stiffness used in the model. Therefore, the small strain model shows the smallest movement.

7. CONCLUSIONS

A comprehensive constitutive model for soil for practical applications has been presented in this paper. The model is based on the multilaminate framework where constitutive relations, such as the yield and plastic potential functions and hardening rules are specified on randomly oriented planes. Therefore, plastic strains develop independently on active planes, i.e. hardening due to loading can occur on some of the planes while others are in unloading or even tension at the same time. Deformation behaviour in the range of very small strains is taken into account by considering two different micromechanics-based contact models, viz. the Hertz–Mindlin contact model and the rough-surface contact model. Degradation of high initial stiffness with the accumulation of shear strains on the respective plane and its dependency on the shear strain history are characterized by mathematical functions of experimental investigations presented in the literature. A successful application of the micromechanics-based formulations has been shown for element tests as well as a boundary value problem. Results from the simulation of a deep excavation showed significant influence of small strain stiffness on the predicted deformations of the retaining wall and settlement profile.

REFERENCES

1. Pande GN, Sharma KG. Multilaminate model of clays—a numerical evaluation of the influence of rotation of principal stress axes. *International Journal for Numerical and Analytical Methods in Geomechanics* 1983; **7**(4):397–418.
2. Schuller H, Schweiger HF. Application of a multilaminate model to simulation of shear band formation in NATM-tunnelling. *Computers and Geotechnics* 2002; **29**:501–524.
3. Pietruszczak S, Pande GN. Multi-laminate framework of soil models—plasticity formulation. *International Journal for Numerical and Analytical Methods in Geomechanics* 1987; **11**(6):651–658.
4. Neher HP, Vermeer PA, Bonnier PG. Strain-rate effects in soft soils modelling and application. In *Proceedings of the 3rd International Conference on Soft Soil Engineering*, Hong Kong, Lee CF, Lau CK, Ng CWW, Kwong AKL, Pang PLR, Yin J-H, Yue ZQ (eds). Balkema: Rotterdam, 2001; 361–367.
5. Wiltafsky Ch. A multilaminate model for normally consolidated clay. *Ph.D. Thesis*, Gruppe Geotechnik Graz, Heft 18, Graz University of Technology, Austria, 2003.
6. Batdorf SB, Budiansky B. A mathematical theory of plasticity based on the concept of slip. *TN 1871*, National Advisory Committee for Aeronautics, 1949.
7. Calladine CR. A microstructural view of the mechanical properties of saturated clay. *Géotechnique* 1971; **21**(4):391–415.
8. Taylor GI. Plastic strain in metals. *Journal of the Institute of Metals* 1938; **62**:307–324 (Reprinted in the Scientific Papers of G. I. Taylor 1. Cambridge University Press: Cambridge, U.K., 1958).
9. Zienkiewicz OC, Pande GN. Time-dependent multilaminate model of rocks—a numerical study of deformation and failure of rock masses. *International Journal for Numerical and Analytical Methods in Geomechanics* 1977; **1**(3):219–247.

DOI: 10.1002/nag

10. Sadrnejad SA, Pande GN. A multilaminate model for sands. In *Proceedings of the 3rd International Symposium on Numerical Models in Geomechanics* (*NUMOG*), Niagara Falls, Canada, Pietruszczak S, Pande GN (eds). Elsevier: London, 1989; 17–27.
11. Brinkgreve RBJ, Broere W, Waterman D. *Plaxis*, *Finite Element Code for Soil and Rock Analyses*, *Users Manual*. PLAXIS b.v.: The Netherlands, 2006.
12. Scharinger F, Schweiger HF. Undrained response of a double hardening multilaminate model for soils. In *Proceedings of the 11th International Conference of the International Association of Computer Methods and Advances in Geomechanics* (*IACMAG*), Turin, Italy, Barla G, Barla M (eds). Patron Editore: Bologna, 2005; 505–512.
13. Scharinger F. A multilaminate model for soil incorporating small strain stiffness. *Ph.D. Thesis*, Gruppe Geotechnik Graz, Heft 31, Graz University of Technology, Austria, 2007.
14. Bažant ZP, Oh BH. Microplane model for progressive fracture of concrete and rock. *Journal of Engineering Mechanics* (ASCE) 1985; **11**(4):559–582.
15. Fliege J, Maier U. A two-stage approach for computing cubature formulae for the sphere. *Ergebnisberichte Angewandte Mathematik No. 139T*, Fachbereich Mathematik, Dortmund University, Germany, 1996.
16. Fliege J, Maier U. The distribution of points on the sphere and corresponding cubature formulae. *IMA Journal of Numerical Analysis* 1999; **19**(2):317–334.
17. Bažant ZP, Oh BH. Efficient numerical integration on the surface of a sphere. *Zeitschrift für Angewandte Mathematik und Mechanik* 1986; **66**:37–49.
18. Duffy J, Mindlin RD. Stress–strain relations and vibrations of a granular medium. *Journal of Applied Mechanics* 1957; **79**:585–593.
19. Deresiewicz H. Stress–strain relations for a simple model of granular medium. *Journal of Applied Mechanics* 1958; **25**:402–406.
20. Digby PJ. The effective elastic moduli of porous granular rock. *Journal of Applied Mechanics* 1981; **48**(4): 803–808.
21. Walton K. The effective elastic moduli of a random packing of spheres. *Journal of the Mechanics and Physics of Solids* 1987; **35**(2):213–226.
22. Chang CS, Sundaram SS, Misra A. Initial moduli of particulated mass with frictional contacts. *International Journal for Numerical and Analytical Methods in Geomechanics* 1989; **13**:629–644.
23. Chang CS, Misra A, Sudaram SS. Properties of granular packings under low amplitude cyclic loading. *Soil Dynamics and Earthquake Engineering* 1991; **10**(4):201–211.
24. Chang CS, Liao CL. Estimates of elastic modulus for media of randomly packed granules. *Applied Mechanics Review* 1994; **47**(1, Part 2):197–206.
25. Yimsiri S, Soga K. Micromechanics-based stress–strain behaviour of soils at small strains. *Géotechnique* 2000; **50**(5):559–571.
26. Yimsiri S, Soga K. Application of micromechanics model to study anisotropy of soils at small strains. *Soils and Foundations* 2002; **42**(5):15–26.
27. Mindlin RD, Deresiewicz H. Elastic spheres in contact under varying oblique forces. *Journal of Applied Mechanics* 1953; **20**(3):327–344.
28. Greenwood JA, Tripp JH. The elastic contact of rough spheres. *Journal of Applied Mechanics* (ASME) 1967; **34**(1):153–159.
29. Johnson KL. *Contact Mechanics*. Cambridge University Press: Cambridge, 1985.
30. Chang CS, Misra A, Sundaram SS. Micromechanical modelling of cemented sands under low amplitude oscillations. *Géotechnique* 1990; **40**(2):251–263.
31. Graton LC, Fraser HJ. Systematic packing of spheres with particular relation to porosity and permeability. *Journal of Geology* 1935; **43**:785–909.
32. Smith WO, Foote PD, Busang PF. Packing of homogeneous spheres. *Physical Review* 1929; **34**:1271–1274.
33. Field WG. Towards the statistical definition of a granular mass. *Proceedings of the 4th Australian and New Zealand Conference on Soil Mechanics*, Wellington, 1963; 143–148.
34. Oda M. Co-ordination number and its relation to shear strength of granular material. *Soils and Foundations* 1977; **17**(2):29–42.
35. Marsal RJ. Mechanical properties of rockfill. In *Embankment–Dam Engineering*, *Casagrande Volume*, Hirschfeld RC, Poulos SJ (eds). Wiley: New York, 1973; 109–200.
36. Yanagisawa E. Influence of void ratio and stress condition on the dynamic shear modulus of granular media. In *Advances in the Mechanics and the Flow of Granular Materials II*, Shahinpoor M (ed.). Gulf Publishing Company: Houston, TX, 1983; 947–960.

DOI: 10.1002/nag

37. Pande GN. Influence of grain shape and size on the behaviour of granular materials. In *Proceedings of the 2nd International Conference on Numerical Methods in Engineering*, *Theory and Applications*, Swansea, U.K., Pande GN, Middleton J (eds). Martinus Nijhoff Publishers: Dordrecht, 1987; C26/1.
38. Gerrard CM, Pande GN. Numerical modelling of reinforced jointed rock masses, I. Theory. *Computers and Geotechnics* 1985; **1**:293–318.
39. Bowden FP, Tabor D. *The Friction and Lubrication of Solids*, *Part II*. Clarendon Press: Oxford, 1964.
40. Janbu N. Soil compressibility as determined by oedometer and triaxial tests. *Proceedings of the 3rd European Conference on Soil Mechanics*, Wiesbaden, vol. 1, 1963; 19–25.
41. Goddard JD. Nonlinear elasticity and pressure-dependent wave speeds in granular media. *Proceedings of the Royal Society of London*, *Series A* 1990; **430**:105–131.
42. von Soos P, Bohac J. Properties of soils and rocks and their laboratory determination. *Geotechnical Engineering Handbook*, vol. 1. Ernst & Sohn: Berlin, 2002; 119–206.
43. Hoque E, Tatsuoka F. Anisotropy in elastic deformation of granular materials. *Soils and Foundations* 1998; **38**(1):163–179.
44. Lade PV, Abelev AV. Characterisation of cross-anisotropic soil deposits from isotropic compression tests. *Soils and Foundations* 2005; **45**(5):89–102.
45. Atkinson JH, Sallfors G. Experimental determination of stress–strain–time characteristics in laboratory and in situ tests. *Proceedings of the 10th European Conference on Soil Mechanics and Foundation Engineering*, vol. 3. Associazione Geotechnica Italiana: Florence, Italy, 1991; 915–956.
46. Ramberg W, Osgood WR. Description of stress–strain curves by three parameters. *Technical Note No. 902*, National Advisory Committee for Aeronautics, Washington, DC, U.S.A., 1943.
47. Seed HB, Idriss IM. Soil moduli and damping factors for dynamic response analyses. *Report No. 70-10*, Earthquake Engineering Research Center, Berkeley, CA, U.S.A., 1970.
48. Jardine RJ, Potts DM, Furie AB, Burland JB. Studies of the influence of non-linear stress–strain characteristics in soil–structure interaction. *Géotechnique* 1986; **36**(3):377–396.
49. Santos JA, Gomes Correia A. Reference threshold shear strain of soil. Its application to obtain an unique strain-dependent shear modulus curve for soil. *Proceedings of the 15th International Conference on Soil Mechanics and Foundation Engineering*, Istanbul, Turkey, Publications Committee of the XV ICSMGE (eds). Balkema: Lisse, 2001; 267–270.
50. Soga K, Nakagawa K, Mitchell JK. Measurement of stiffness degradation characteristics of clays using a torsional shear device. In *Proceedings of the 1st International Conference on Earthquake Geotechnical Engineering*, Tokyo, Japan, Ishihara K (ed.). Balkema: Rotterdam, 1995; 107–112.
51. Richardson D. Investigations of threshold effects in soil deformations. *Ph.D. Thesis*, City University, London, U.K., 1988.
52. Kohata Y, Tatsuoka F, Wang L, Jiang GL, Hoque E, Kodaka T. Modelling the non-linear deformation properties of stiff geomaterials. *Géotechnique* 1997; **47**(3):563–580.
53. Desrues J, Zweschper B, Vermeer PA. Database for tests on Hostun RF sand. *Institutsbericht No. 13*, Institute for Geotechnical Engineering, University of Stuttgart, 2000.
54. Lama RD, Vutukuri VS. *Handbook on Mechanical Properties of Rocks*. Trans Tech Publications: Aedermannsdorf, 1978.

DOI: 10.1002/nag